Supplementary Information

High-dimensional multiplexed metamaterial for cross-media all-sound communication

Kai Wu,[†a] Jing-Jing Liu,[†*a] Hao-Xiang Li,[b] Xue-Feng Zhu,[c] Bin Liang,[*a] Jian-Chun Cheng[*a] and Johan Christensen[*d]

[a]*Collaborative Innovation Center of Advanced Microstructures and Key Laboratory of Modern Acoustics, MOE, Institute of Acoustics, Department of Physics, Nanjing University, Nanjing 210093, China*

Email: liujingjing@nju.edu.cn, liangbin@nju.edu.cn, jccheng@nju.edu.cn

[b]*College of Information Science and Technology & College of Artificial Intelligence Nanjing Forestry University, Nanjing 210037, China*

[c]*School of Physics and Innovation Institute, Huazhong University of Science and Technology, Wuhan 430074, China*

[d]*IMDEA Materials Institute, Calle Eric Kandel, 2, Getafe, Madrid 28906, Spain*

E-mail: johan.christensen@imdea.org

[†]Kai Wu and Jing-Jing Liu contributed equally to this work.

Supplementary Note 1. The structural design of the HDM metamaterial

To realize the high transmission efficiency and flexible demodulation of cross-media sound signals, we design a water-air coupling high-dimensional multiplexed (HDM) metamaterial with a three-layered configuration formed by slotting in an acoustically-rigid cube with rationally designed air channels, as illustrated in Fig. S1a. The gray part represents the acoustically rigid material that can be easily implemented with natural materials, and the blue parts are filled with air. In such a design, the layers a and c serving as impedance-matching layers contact with air and water, respectively, and the layer b can introduce a tunable and linear phase shift by changing its length L_b. According to the effective medium method theory, we can easily derive the criterion for realizing the total transmission between air and water

$$\begin{cases} h_a = \lambda_a/4, \ Z_a = \sqrt{Z_{air} Z_b} \\ Z_b = \sqrt{Z_{air} Z_{water}} \\ h_c = \lambda_c/4, \ Z_c = \sqrt{Z_b Z_{water}} \end{cases} \quad \text{* MERGEFORMAT (S1)}$$

where Z_{air} and Z_{water} are the impedance of air and water, h_a and h_c are the thickness of layers a and c, Z_a to Z_c are the acoustic impedance for layers a and c, respectively. The effective acoustic impedance of each layer can be characterized by $\rho_{air} c_{air}/w_i$ (i = a, b, c), which can be freely modulated by changing the width of each layer w_i. However, the transmission efficiency of the designed structure is far lower than expected because the high-order modes near the structure-water interface dramatically alter the near-field interaction with the incident wave and generate an additional huge acoustical reactance. Considering the huge contrast of acoustic impedance between water and air, the additional acoustical reactance cannot be compensated by merely reducing the channel length as in conventional designs. This phenomenon can be alleviated by increasing the radiation area. To this end, we redesign layer c as illustrated in Fig. S1b to increase the radiation area while keeping its impedance matching unimpaired. Due to the redesign of layer c, it is necessary to modulate the parameters of the three layers based on Eq. (S 1). Then, based on this design, we further increase the number of subunits in the unit cell and optimize the structural parameters to eliminate the resonant coupling between them to realize frequency multiplexing. In the current study, we design a dual-frequency-multiplexed unit cell working at 12 kHz and 16 kHz as shown in Fig. S1c. The specific structural parameters are listed in Table S1.

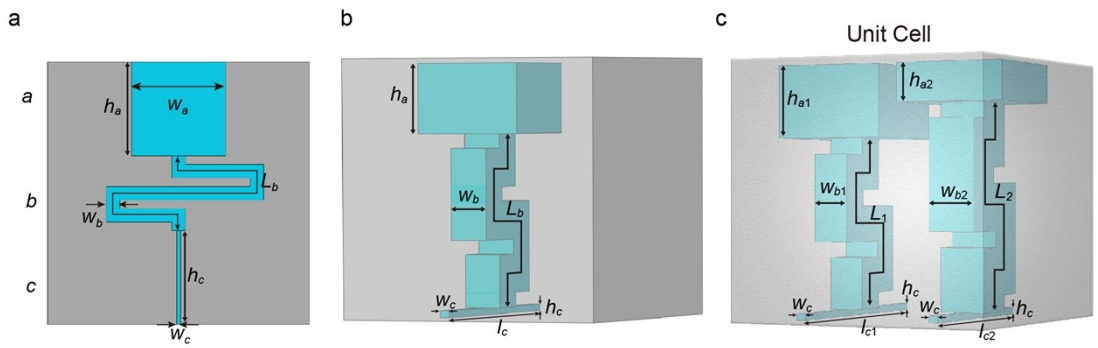

Fig. S1. a) Three-layered design of HDM metamaterial for simultaneously realizing impedance matching and phase modulation at the water-air interface. b) Configuration of the designed three-dimensional HDM metamaterial with one subunit. c) Configuration of the designed three-dimensional HDM metamaterial with two subunits.

Table S1. Specific structural parameters of the designed HDM metamaterial unit in Fig. S1c

Parameter	W	H	w_a	h_{a1}	w_{b1}	l_{c1}	h_c	w_c	h_{a2}	w_{b2}	l_{c2}
unit (mm)	20	19	8.5	5.7	2.7	16.8	0.5	0.7	2.7	3.5	13.5

Supplementary Note 2. The increase in the number of frequency channels

In the current system, for facilitating the experiment, we design a simple water-air coupling HDM metamaterial composed of two subunits to realize two frequency channels multiplexing. We can increase the state density of the hybrid water-air coupling meta-structure to boost the number of frequency channels in the communication system. As a verification, we design an HDM metamaterial unit working at 8 kHz, 12 kHz and 16 kHz, and verify its high transmission efficiency and linear phase shift through numerical simulations, as shown in Fig. S2. The newly designed HDM metamaterial composed of three subunits is schematically illustrated in Fig. S2a, and its structural parameters are listed in Table S2. Next, we demonstrate the ability of this HDM metamaterial to independently relay and modulate the cross-media signal at three frequencies, as shown in Fig. S2b. By adjusting the parameter L_i (i = 1, 2, 3), the designed hybrid meta-structure can produce the phase shift within the range of $-\pi$ to π at corresponding frequency f_i while maintaining high transmission efficiency. Figure S2c shows the resulting intensity enhancement (IE) and phase shift at different frequencies in response to the varying structural parameter L_i. Notice that here we only

demonstrate the amplitude and phase modulation ability of each subunit while keeping the parameters of the other two subunits fixed. In fact, the frequency selectivity of each subunit ensures that the relay and demodulation ability of a specific subunit is not affected by changing the parameters of the other two subunits.

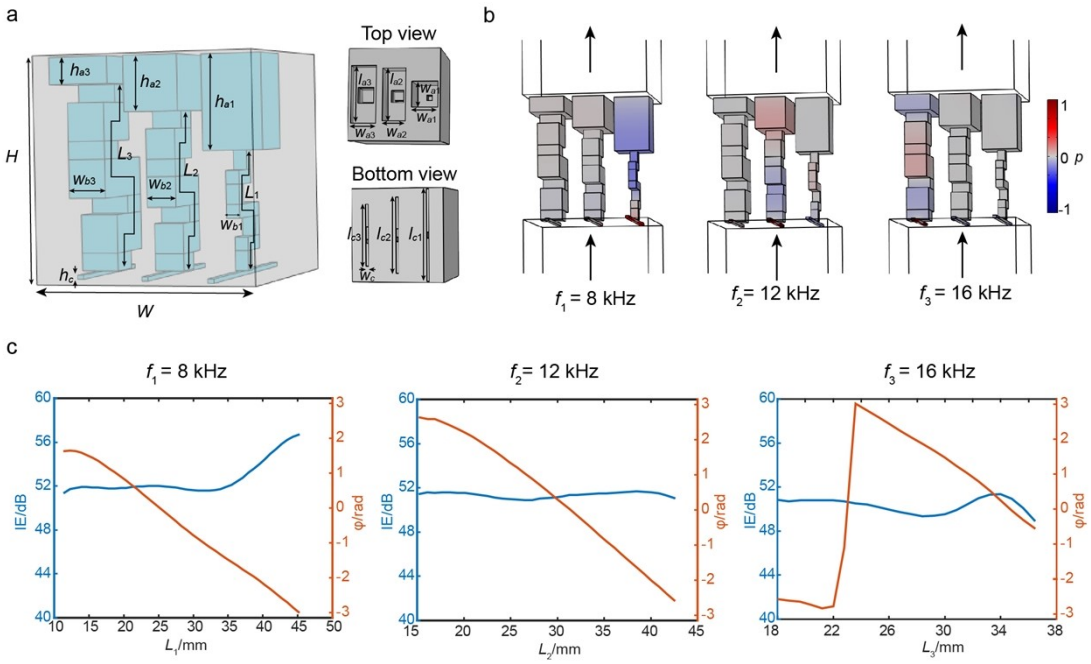

Fig. S2. a) Configuration of the designed HDM metamaterial with three subunits. b) The acoustic pressure fields in the whole HDM metamaterial unit at f_1 = 8 kHz, f_2 = 12 kHz, and f_3 = 16 kHz, respectively. The arrows indicate the incident and transmission directions. c) Simulated intensity enhancement (IE) and phase shift provided by the unit with different structural parameter L_i.

Table S2. Specific structural parameters of the designed HDM metamaterial unit in Fig. S2

Parameter	W	H	w_{a1}	h_{a1}	w_{b1}	l_{c1}	h_c	w_c	w_{a2}
unit (mm)	21	21	5.9	9.1	1.3	20.5	0.4	0.6	5.33
Parameter	l_{a2}	h_{a2}	w_{b2}	l_{c2}	w_{a3}	l_{a3}	h_{a3}	w_{b3}	l_{c3}
unit (mm)	12	5.3	2.9	17	5.87	13.2	2.6	3.7	14

Supplementary Note 3. The analysis of the influence of phase discretization on the OAMs demultiplexing

Due to the finite size of an individual unit, continuous phase profiles desired for producing various wave fields (including those with extremely complicated spatial

patterns like acoustic holograms) have to be discretized, which also simplifies the design and facilitates the fabrication of a prototype. Similarly, to avoid continuously varying the structural parameters of each unit, in the current design, we use a 2nd-order discrete phase to replace the ideal phase, which can provide a sufficient degree of freedom to enable effective beam manipulation while maintaining a high quality of the modulated field. In our experiment, we employed four basic HDM metamaterial units with different combinations of (L_1, L_2) values: (17 mm, 31.2 mm), (17 mm, 18.4 mm), (32.2 mm, 31.2 mm) and (32.2 mm, 18.4 mm)) marked by four dots in Fig. 2c to achieve two equally spaced steps of phase shift (0, π) at two operating frequencies. For clearer illustration, we also simulate the acoustic pressure distribution through the above four basic units and plot the results in Fig. S3, which shows the desired phase shift with the change of L_1 and L_2 as well as a high transmission efficiency over 70 %.

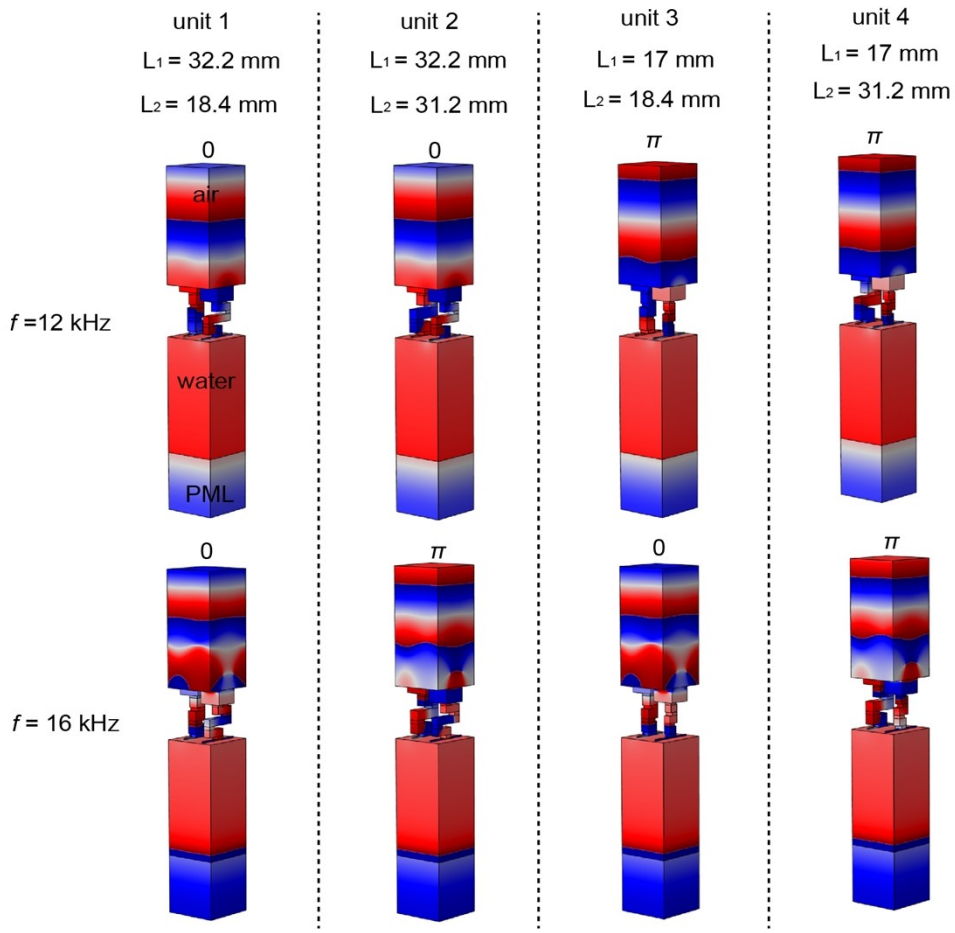

Fig. S3. Simulated sound transmission through four basic building blocks at two frequencies, corresponding to four phase shift combinations required in the current design.

Next, we numerically demonstrate the feasibility of using 2-order phase

discretization in our scheme. Figure S4a shows the ideal phase profiles for demultiplexing two-mode vortex beams at 12 kHz and 16 kHz, respectively, as proposed in the main text, along with several discrete phase profiles with different orders of phase discretization (defined as N). In Fig. S4b, we plot the typical results of sound intensity distributions on the receiving plane when two OAM channels are opened simultaneously, and no appreciable difference is observed as N varies. These results demonstrate the high robustness of our meta-repeater against phase discretization and confirm the feasibility of using 2-order discrete phase in our design.

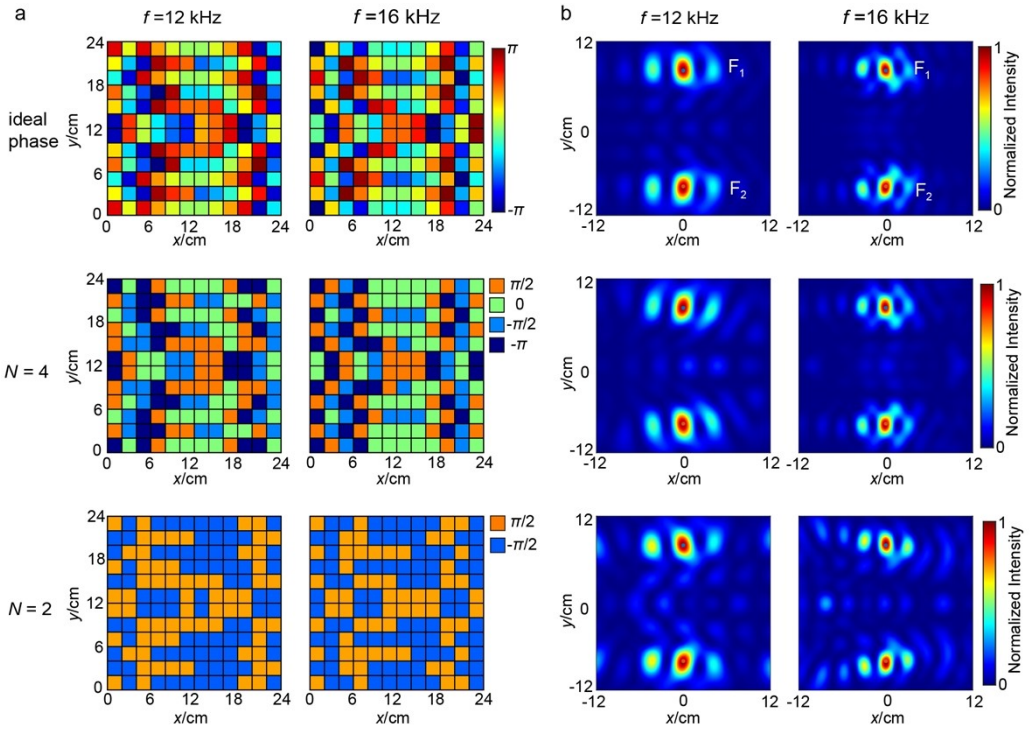

Fig. S4. a) Ideal continuous phase profile and discrete phase profiles with different orders of phase discretization N for the two-mode two-frequency communication system in the main text. b) Simulated normalized sound intensity distributions on the output plane when turning on two OAM channels simultaneously at two frequencies respectively, corresponding to the phase profiles in a).

Supplementary Note 4. Encoding information into the multiplexed acoustic vortex beams using an active underwater transducer array

At the transmitting terminal, we establish a multi-mode OAM multiplexing system using a Field-Programmable Gate Array (FPGA)-driven transducer array. The array consists of 8 underwater acoustic transducers evenly arranged on a circle with a diameter of 190 mm, as shown in Fig. S5a. The relative phases of the transducers used

to emit *l*th-order vortex beam are determined by $\varphi = l\theta$, where θ is the azimuthal angle between the transducer and a reference point. The multiplexing of vortex beams with different OAM modes is accomplished by controlling the phase and amplitude of each transducer through the required signals fed into the FPGA. Figure S5b depicts the relative phases of driven signals of eight transducers that generate the synthesized vortex beams of l_1 = +1 and l_2 = -1, where the eight driven signals have identical amplitude. In our experiment, eight relays are employed to control the input signals of each transducer to be "on" or "off", which encode "0" and "1" data streams onto the amplitude of vortex beams through binary amplitude-shift keying (2ASK) digital modulation technology. These relays are controlled by a single-chip microcomputer (SCM), and the transmitted data streams serve as the input signals of the SCM.

a

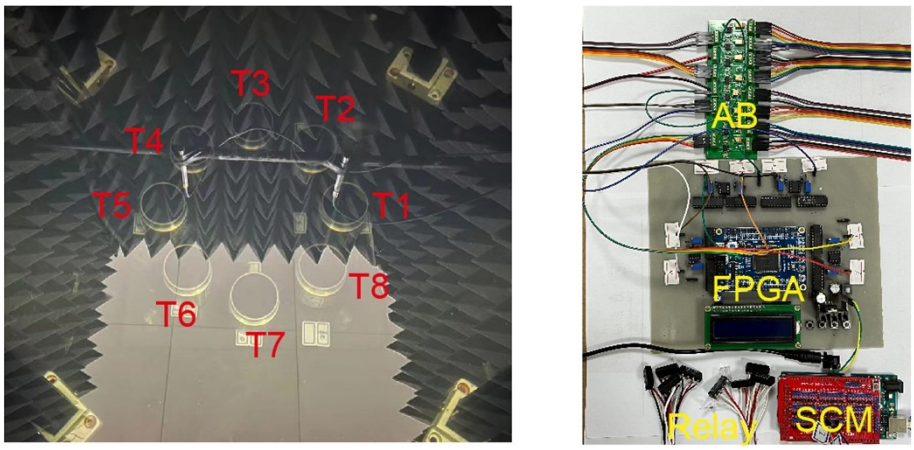

b

	T1	T2	T3	T4	T5	T6	T7	T8
φ/rad	0	$7\pi/4$	$2\pi/4$	$5\pi/4$	$4\pi/4$	$3\pi/4$	$6\pi/4$	$\pi/4$

Fig. S5. Active transducer array used in our experiment. a) The FPGA on the left drives eight underwater acoustic transducers marked by T1-T8 on the acrylic glass frame. Eight relays controlled by a SCM are used to modulate eight input signals from the FPGA to be "on" or "off" respectively. b) The relative phases of the input signals of eight underwater acoustic transducers.

Supplementary Note 5. The measured sound distributions on the output plane without the HDM metamaterial at the water-air interface

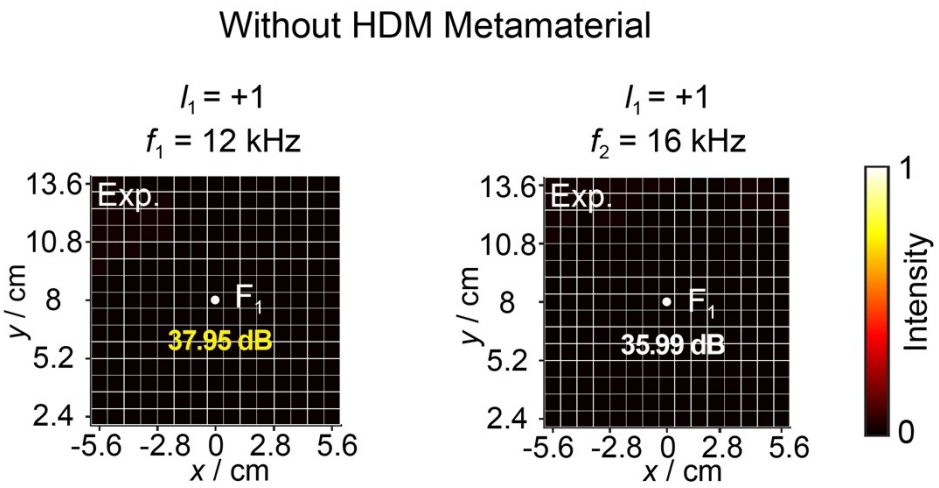

Fig. S6. The measured sound intensity distributions of the square area centered at F_1 when transmitting the vortex beam of l_1 = +1 at f_1 and f_2, respectively, in the case of the bare water-air interface.

Supplementary Note 6. The realization of a higher transmission speed of our proposed cross-water-air all-sound communication system

There are many factors that can impact the communication speed, such as operating frequency, the pulse modulation period, the number of channels and the modulation technology applied. For simplicity while without losing generality, in the main text, we showcase an experiment using a four-channel communication system that includes two coaxially overlapped vortex beams at two operating frequencies. To open up more channels, we can increase the number of operating frequencies and the number of OAM modes in each path. For instance, by redesigning the phase mask with no need to change the frequency number, the proposed mechanism can realize effective mode separation and decoding for more OAM modes, as evidenced by the OAM demultiplexing results for an upgraded two-frequency four-mode system across the water-air interface shown in Fig. S7. At two operating frequencies, the focal points of vortex beams with OAM modes of +1, -1, -2, and +2 are set at F_1 (0, 0.17 m, 0.631 m), F_2 (0, -0.17 m, 0.631 m), F_3 (-0.103 m, 0, 0,631 m) and F_4 (0.103 m, 0, 0.631 m) respectively. Based on this, the binary phase distributions of the meta-repeater at two frequencies are illustrated in Fig. S7a, and the final frequency-multiplexed meta-repeater is constructed by combining the phase distributions at 12 kHz and 16 kHz. To prove the effectiveness of this

communication system, we plot in Fig. S7b, c the simulated sound intensity distributions on the output plane when turning on a single channel and four channels respectively, which manifest the ability of the designed meta-repeater to separate and focus the vortex beams with different OAM modes into their predesigned focal points.

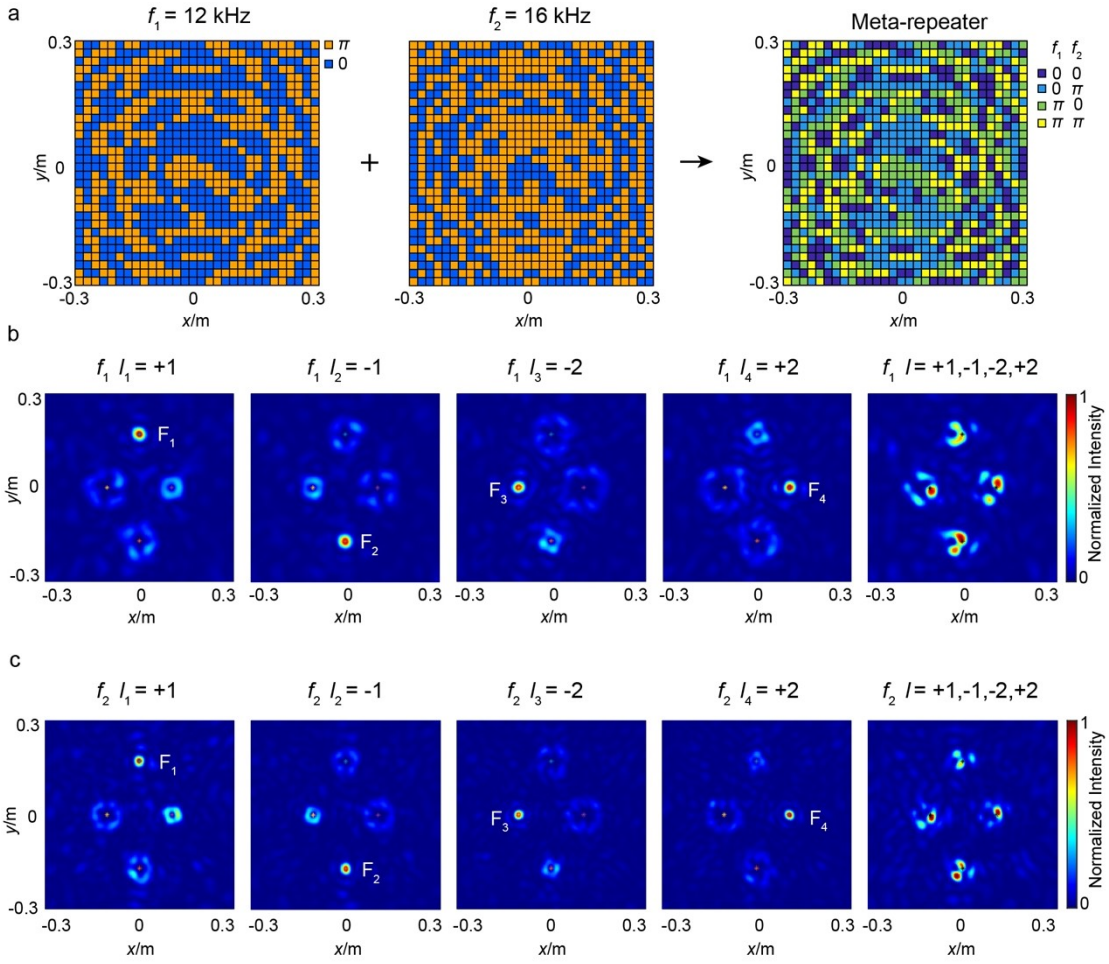

Fig. S7. a) The binary phase profiles required for the meta-repeater to demultiplex the four-mode OAM beams (-2, -1, +1, +2) at f_1 and f_1 respectively, and the final phase distribution of the frequency-multiplexed meta-repeater. b, c) The demultiplexing results of the meta-repeater for four-mode vortex beam when different OAM channels are opened.

Furthermore, the communication speed can also be improved by applying the higher-order modulation technique or reducing the pulse modulation period. To further assess the effectiveness of our mechanism under the condition of shorter pulses, we performed additional measurements using a shorter pulse period of T_0 = 0.8 ms (i.e., half of the original value) while keeping all other experimental conditions unchanged. In such a

case, we transmitted the same 4-bit grayscale image as in the main text through four independent channels in parallel, corresponding to a bit rate of 5 kbit/s for 2ASK modulation. As shown in Fig. S8, the received time-domain signals and the corresponding decoded data stream (red dots) exhibit exact agreement with the input sequence (blue line) over an arbitrarily chosen interval. Consistently, the meta-repeater-based demultiplexing and communication across the water-air interface remain correct for all multiplexed channels, and no bit errors are observed in the decoded image (BER = 0). This demonstrates that the proposed cross-media communication system can tolerate relatively shorter pulse periods without compromising decoding accuracy, at least down to 0.8 ms in our design.

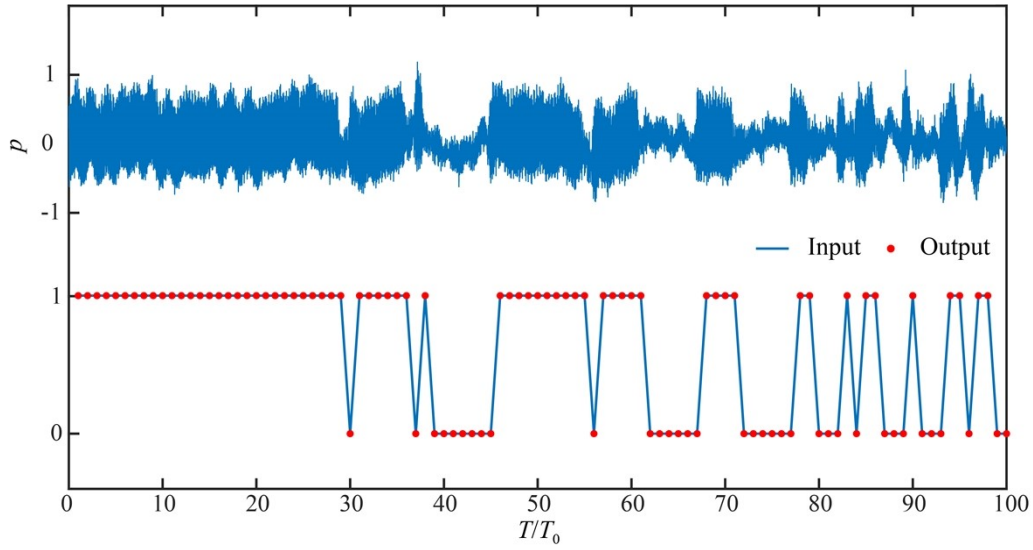

Fig. S8. The measured time-domain waveform over successive pulse periods and the corresponding output data stream, compared with the input bit sequence.

Supplementary Note 7. Robustness analysis under realistic sea-surface conditions

In addition to the surface fluctuation considered in our experiments, other practical factors such as volume turbulence and multipath propagation can also perturb the wave propagation and thereby affect cross-media communication performance. The robustness analyses of our mechanism under representative real-world conditions are as follows:

1. Fluctuating interface: In the main text, we have already inspected the robustness of our mechanism against interface fluctuation by performing a communication test under a deliberately fluctuating interface with relatively low interface roughness ($\sigma/\lambda_w < 0.1$, σ is the root-mean-square amplitude of the surface wave and λ_w is the

wavelength in water). The water–air interface was intentionally disturbed to generate random, irregular surface waves, which can induce certain perturbations in both phase and amplitude profile of the outgoing wave but not completely destroy the wavefront. The measured BER of the four multiplexed channels remaining as low as 2.5×10^{-4} confirms that such weak interface fluctuation does not influence the performance of our mechanism. To further inspect the system's performance under stronger surface roughness, we consider a simple random rough-surface model based on classical scattering theory.[1] In this model, the effect of nonplanarity of the water-air interface can be equivalently regarded as a random phase screen imposed on the meta-repeater. The interface fluctuation distribution $\eta(x, y)$ is modeled as a zero-mean Gaussian random field with RMS value σ and Gaussian autocorrelation

$$\langle \eta(\mathbf{r})\eta(\mathbf{r}+\boldsymbol{\rho}) \rangle = \sigma^2 \exp(-\rho^2 / L_c^2) \text{ * MERGEFORMAT (S2)}$$

where L_c is the lateral correlation length. For near-normal incidence, the phase perturbation induced by the interface fluctuation takes the following form

$$\Delta\phi(x, y) = k_{\text{eff}}\eta(x, y) \qquad \text{* MERGEFORMAT (S3)}$$

where the effective wavenumber $k_{\text{eff}} \approx 2k_w = 4\pi/\lambda_w$. In the simulations, to consider the impact of roughness-induced phase fluctuations on demultiplexing, the ideal phase profile $\phi_0(x, y)$ calculated by Eq. (2) in the main text is replaced by $\phi(x, y) = \phi_0(x, y) + \Delta\phi(x, y)$. To analyze a rougher surface than that in our tank experiment, we set σ = 15 mm ($\sigma/\lambda_w > 0.1$) and L_c = 50 mm, which corresponds to centimeter-scale surface undulations. Figure S9 shows the phase perturbation distributions for 12 kHz and 16 kHz, as well as the corresponding demultiplexing results when different OAM channels are opened, respectively. It can be observed that the energy distribution on the detection plane is disturbed to a certain extent, while obvious energy convergence at the target focal points and suppression at non-target points remain clearly visible, indicating that the demultiplexing mechanism is still robust to this level of surface roughness.

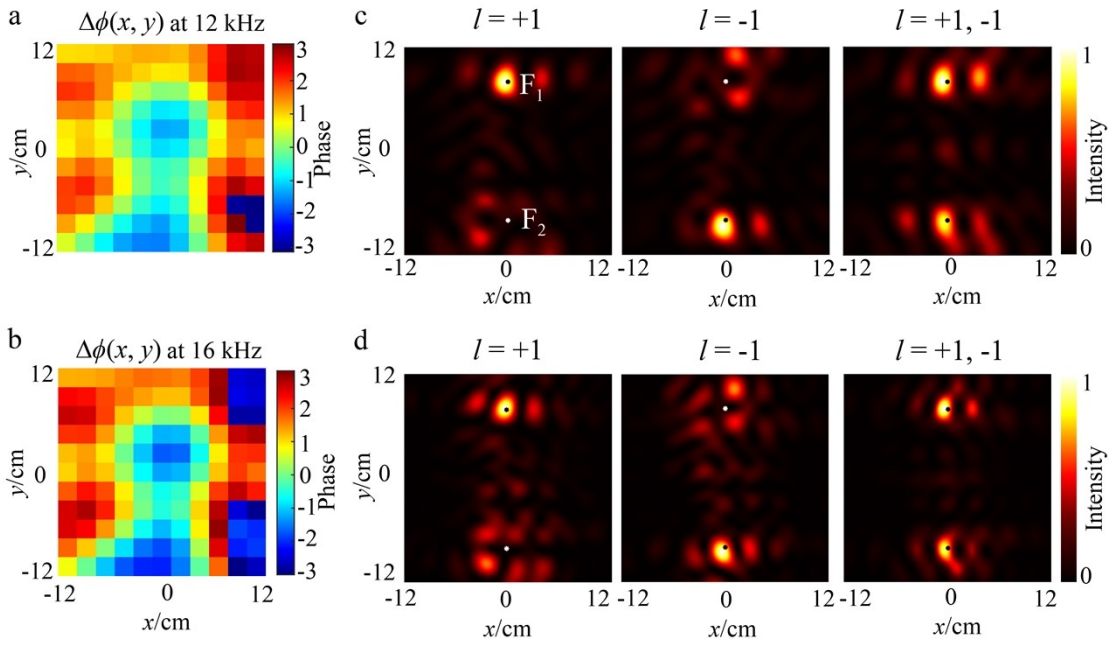

Fig. S9. The phase perturbation distributions imposed on the meta-repeater phase profile at a) 12 kHz and b) 16 kHz, respectively. The corresponding simulated acoustic intensity distributions on the detection plane at c) 12 kHz and d) 16 kHz when different OAM channels are opened, respectively.

2. Turbulence: Beyond surface roughness, another typical fact, underwater turbulence, may also distort the wavefronts and impair the vortex beam's phase structure. To evaluate the influence of turbulence effects, here we use a multiple random phase-screen model.[2] In the following analysis, we extend the propagation distance to $50\lambda_w$ at each operating frequency while keeping the remaining configuration consistent with the experiment. Along the propagation path, five phase screens (24 × 24 cm^2) are equidistantly inserted to mimic the effect of turbulence. The oceanic turbulence parameters used in the random phase-screen model are set as follows: the rate of dissipation of kinetic energy per unit mass of fluid ε = 0.01 m^2/s^3, the Kolmogorov micro scale η = 10^{-3} m, the rate of dissipation of mean-squared temperature χ_T = $10^{-6.5}$ K^2/s and the ratio of temperature and salinity contributions to the refractive index spectrum ω = -4.[3] Figure S10a illustrates the phase distribution of one random phase screen with an RMS phase value of 0.3 rad. For clear illustration, we showcase in Fig. S10b the simulated field distributions of a 1st-order vortex beam after propagating through five phase screens, where both the helical phase structure and the donut-shaped amplitude profile are remarkably

degraded by turbulence. To evaluate its impact, we then numerically calculate the sound intensities at the two focal points when different channels are opened at 12 kHz and 16 kHz in the presence of turbulence, and plot the histograms of sound intensity in Fig. S11. The results reveal an intensity contrast ratio exceeding 30 dB at the detection points between the "on" and "off" states of each channel, which demonstrates that the demultiplexing performance and the reliability of the received signals are still maintained despite the strong turbulence conditions.

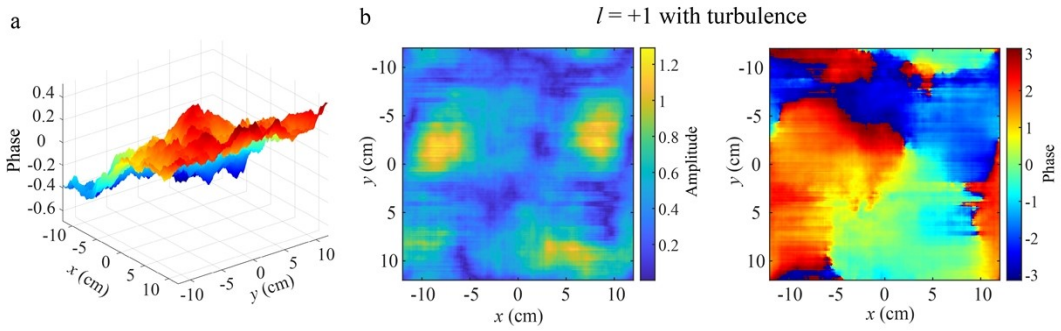

Fig. S10. a) The phase distribution of one random phase screen. b) The sound field distributions of the 1st-order vortex beam after propagating $50\lambda_w$ with ocean turbulence.

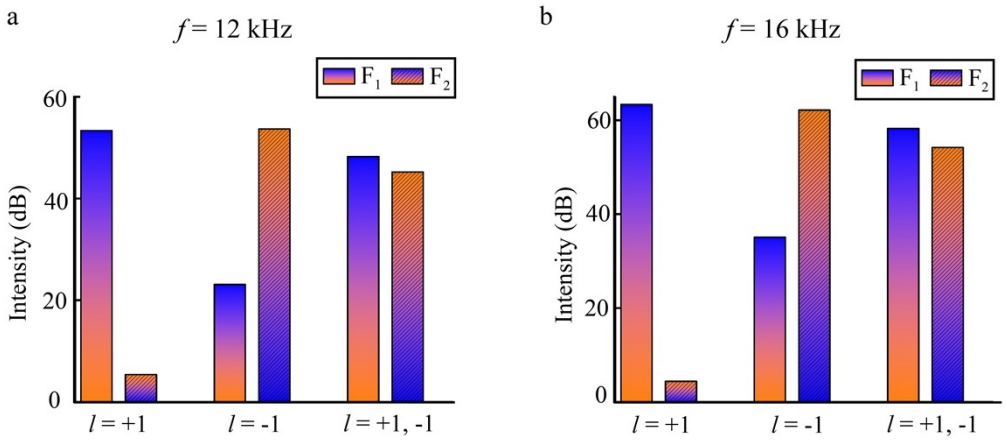

Fig. S11. The histograms of simulated sound intensity at two focal points in the presence of turbulence when different OAM channels are opened at a) 12 kHz and b) 16 kHz.

3. Multipath effect: The multipath effect in underwater acoustic propagation arises from surface and bottom reflections, refraction induced by sound-speed gradients, and scattering caused by environmental inhomogeneities. Multipath components

generally arrive with different incident angles and time delays. In our configuration, the meta-repeater exhibits strong spatial selectivity and is primarily responsive to waves incident within a limited angular range around the designed direction. To quantitatively characterize this directional selectivity, we rotate the OAM emitter to vary the incidence direction of a single-mode vortex beam and plot the simulated intensity at the focal points as a function of the rotation angle in Fig. S12. For all four single-mode cases, the angular response exhibits a clear main lobe with a full width at half maximum of approximately 20°. This strong spatial selectivity yields the most multipath components that are angle-mismatched to appear as a defocused, lower-amplitude background noise at the focal points rather than producing strong coherent replicas that would cause severe inter-channel crosstalk. This implies that by appropriately adjusting the orientation of the receiver, we can selectively capture the transmitted signal arriving from a specific direction while spatially filtering out multipath components from other directions, thereby effectively suppressing the impact of multipath effects.

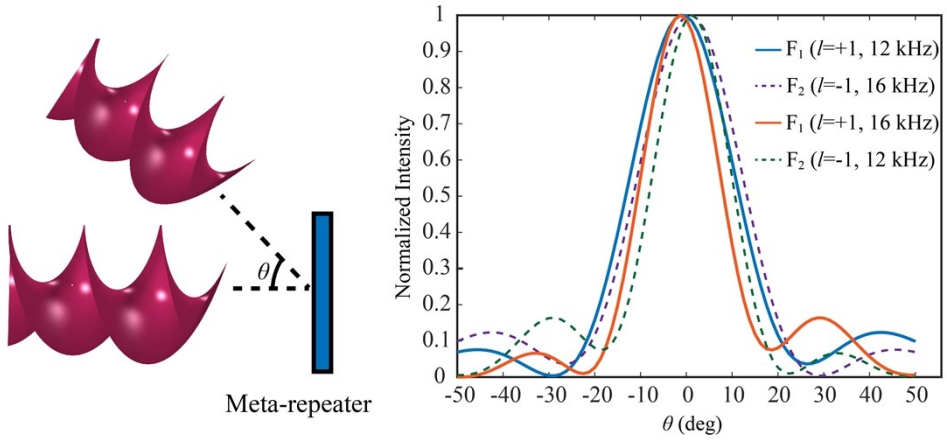

Fig. S12. The simulated normalized sound intensity at two focal points versus incident angle θ for four single-mode cases.

The above analyses demonstrated the strong robustness of our proposed HDM metamaterial-based all-sound communication system against representative practical factors. There are also some methods capable of further improving the robustness of our methodology. For example, by reshaping the spatial profile of the vortex beam into a Bessel-Gaussian form, it can exhibit the exceptional property of partial self-healing, which helps mitigate the influence of volume scattering.[4] In addition, it is worth noting that our proposed mechanism is also compatible with existing communication

techniques. Consequently, some advanced signal-processing methods, such as phase-retrieval algorithms, guard intervals, channel equalization, and forward-error correction, can be readily incorporated to further enhance the robustness and stability of our system.

Supplementary Note 8. The realization of km-scale all-sound communication across the water-air interface

Due to the limited experimental space in an anechoic water tank, we only experimentally demonstrated the effectiveness of our proposed mechanism under a relatively short transmission distance. Here, we give further investigation on the potential of our mechanism to enable high-capacity communication across water-air interface at a distance much longer than the current optical technology of underwater communication without enlarging unlimitedly the arrays for sending and receiving signals. And the transmission distance in air can also be increased by reasonably designing the focus position and optimizing the transverse size of the active phase array and the meta-repeater.

To verify the effectiveness of our mechanism, we perform numerical simulations demonstrating frequency-multiplexed and OAM-multiplexed all-sound communication across the water-air interface over a km-scale underwater distance and an applicable transmission distance in air. The transverse sizes of the active phased array and the meta-repeater are designed as 3.6 m × 3.6 m, and the underwater transmission distance is 1600 m. This transmission distance exceeds the longest underwater optical communication distance realized by using blue-green laser with a small absorption and scattering coefficient in a clear oceanic medium. At the water-air interface, we redesign the meta-repeater for this long-distance communication system, and the two-frequency two-mode synthesized vortex beams are effectively transmitted from water to air and simultaneously demultiplexed and focused into the expected detection points, i.e., F_1 (0, 1.6 m, 125 m) for OAM mode l = +1 at 12 kHz and 16 kHz, F_2 (0, -1.6 m, 125 m) for OAM mode l = -1 at 12 kHz and 16 kHz. To prove the effectiveness of this communication system, we calculate the sound intensity at two focal points under all encoding circumstances of two OAM modes at two frequencies and plot the histograms of normalized sound intensity in Fig. S13a. The results show that the sound intensity difference between channel “on” and “off” exceeds 17 dB, which guarantees the low bit error rate (BER) in the practical implementation of the OAM-based all-sound

communication across the water-air interface at two working frequencies. For clearer illustration, we also plot in Fig. S13b the simulated sound intensity distributions on the output plane when turning on different channels at two frequencies respectively, which manifest the ability of meta-repeater to separate and focus the vortex beams with different OAM modes into predesigned focal points. Therefore, by optimally choosing the size of the source array and meta-repeater, and reasonably designing the detection positions for the vortex beams, we have achieved an underwater propagation distance of up to km-scale and a distance in air of up to 125 m. This allows for the decoding and receiving of signals through unmanned aerial vehicles or other flying objects.

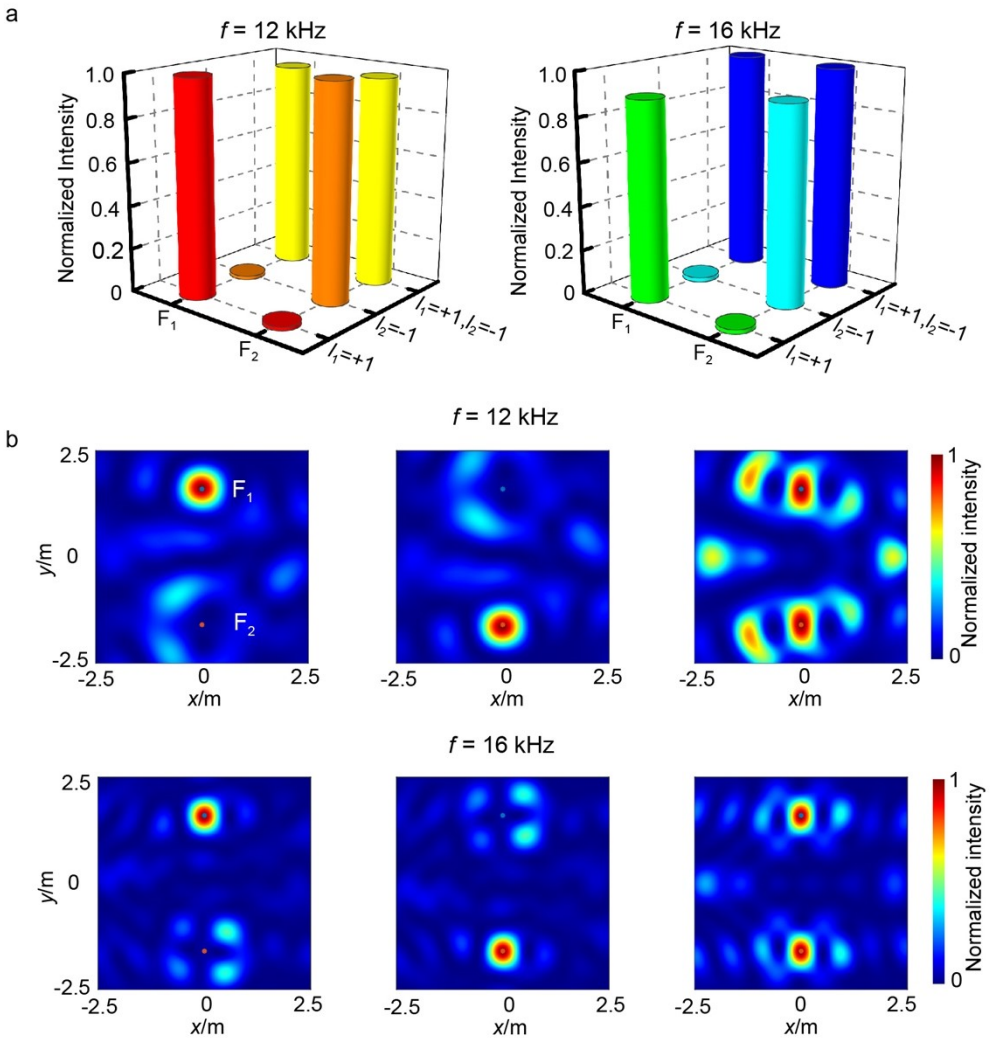

Fig. S13. a) Histograms of normalized sound intensity at two focal points when turning on different channels at two frequencies, respectively. b) The simulated sound intensity distributions on the output plane when turning on different channels at two frequencies, respectively.

Table S3. Comparison between our work and representative literature in terms of controllable dimensions, transmission efficiency, bandwidth, and communication capability.

	Controllable Dimensions	Transmission enhancement	Bandwidth	Communication Scheme
Our work	Amplitude + Phase + Frequency + OAM	~30 dB	11.2-12.8 kHz 15.6-16.4 kHz	Multi-frequency × Multi-OAM multiplexing
Phys. Rev. Lett. 120, 044302 (2018) (Ref. 21 in the main text)	Amplitude	~20 dB	~700 Hz	None
Research 2021, 9757943 (2021) (Ref. 24 in the main text)	Amplitude	>20 dB	10–4000 Hz	None
Appl. Phys. Lett. 123, 231703 (2023) (Ref. 26 in the main text)	Amplitude + Frequency	>20 dB	380–510 Hz	None
Adv. Mater. 35, 2301799 (2023) (Ref. 27 in the main text)	Amplitude + Phase	38 dB	8 kHz	None
Adv. Sci. 10, 2207181 (2023) (Ref. 28 in the main text)	Amplitude + Phase + OAM	25.9 dB	10 kHz	None
Eng. Struct. 341, 120611 (2025) (Ref. 31 in the main text)	Amplitude + Frequency	22 dB	8-9.5 kHz	Frequency Shift Keying (not multiplexing)

Table S4. Comparison between our work and three representative cross-water-air communication approaches (acoustic-to-RF relay-based systems, laser-induced photoacoustic links, and hybrid acoustic–optical surface-readout links) in terms of data rate, carrier type, latency characteristics, hardware complexity, and robustness.

	Data rate	Carrier type	Latency	Hardware Complexity	Robustness
All sound (our work)	High	One	Low	Low	High
Relay-based	Low	Two	High	High	High
Laser-induced sound	Low	Two	Low	Moderate	Low
Acoustic-induced vibration	Low	Two	Low	Moderate	Low

References

1 E. I. Thorsos, *J. Acoust. Soc. Am.*, 1988, **83**, 78-92.

2 S. Pan, L. Wang, W. Wang and S. Zhao, *Sci. Rep.*, 2019, **9**, 14009.

3 H. Chang, X. Yin, X. Cui, X.-Z. Chen, Y.-Z. Su, J.-X. Ma, Y.-J. Wang, L. Zhang and X. Xin, *Appl. Opt.*, 2019, **58**, 6085-6090.

4 S. Li and J. Wang, *Sci. Rep.*, 2017, **7**, 43233.